Template-stabilized oxidic nickel oxygen evolution catalysts

Nancy Li[a], Thomas P. Keane[a], Samuel S. Veroneau[a], Ryan G. Hadt[b,c], Dugan Hayes[b,d], Lin X. Chen[b,e], and Daniel G. Nocera[a,1]

[a]Department of Chemistry and Chemical Biology, Harvard University, Cambridge, MA 02138; [b]Chemical Sciences and Engineering Division, Argonne National laboratory, Lemont, IL 60439; [c]Division of Chemistry and Chemical Engineering, California Institute of Technology, Pasadena, CA 91125; [d]Department of Chemistry, University of Rhode Island, Kingston, RI 02881; and [e]Department of Chemistry, Northwestern University, Evanston, IL 60208

Earth-abundant oxygen evolution catalysts (OECs) with extended stability in acid can be constructed by embedding active sites within an acid-stable metal-oxide framework. Here, we report stable $NiPbO_x$ films that are able to perform oxygen evolution reaction (OER) catalysis for extended periods of operation (>20 h) in acidic solutions of pH 2.5; conversely, native NiO_x catalyst films dissolve immediately. In situ X-ray absorption spectroscopy and ex situ X-ray photoelectron spectroscopy reveal that PbO_2 is unperturbed after addition of Ni and/or Fe into the lattice, which serves as an acid-stable, conductive framework for embedded OER active centers. The ability to perform OER in acid allows the mechanism of Fe doping on Ni catalysts to be further probed. Catalyst activity with Fe doping of oxidic Ni OEC under acid conditions, as compared to neutral or basic conditions, supports the contention that role of Fe^{3+} in enhancing catalytic activity in Ni oxide catalysts arises from its Lewis acid properties.

water-splitting catalysis | renewable energy | solar to fuels | electrocatalysis | acid-stable templating

Widespread implementation of solar energy requires the utilization of efficient energy storage systems that manage the diurnal nature of solar sources (1–4). Hydrogen storage coupled with fuel cells (5), and electrochemical water electrolysis to generate oxygen and hydrogen coupled to CO_2 fixation (6, 7) offer portable solutions to energy storage. Of the two water-electrolysis half reactions, the oxygen evolution reaction (OER) is more kinetically demanding because it requires the transfer of four protons coupled with four electrons from two water molecules to produce a single oxygen molecule (8–10).

A variety of earth-abundant metal oxides have been developed to operate OER in both neutral and basic pH regimes (11–19), but they are unstable in acid, undergoing rapid dissolution into soluble metal ions. The development of oxygen-evolving catalysts (OECs) that operate in acid is desirable in the application of electrolyzers (20, 21) and selected photoelectrochemical devices (22, 23), due to the creation of locally acidic environments by Nafion membranes and requisite acidic pH for silicon-based photovoltaic material stability, respectively. IrO_2 and RuO_2 have high activity for OER and long-term stability in acid but they are composed of critical metals thus prohibiting their widespread adoption (24, 25). Efforts have been made to enhance MnO_x films, which form stable oxides in low-pH regimes (26), for OER through potential cycling deposition (27, 28). These films, however, do not operate at high current densities for extended periods of time owing to phase and compositional transitions of the manganese oxide lattice. To develop a robust and active catalyst for OER in acid using earth-abundant metals, we have pursued a mixed-metal-oxide design strategy with each metal oxide serving an independent role to optimize stability and activity. We have previously demonstrated this design concept with the development of $CoFePbO_x$ which satisfies the criteria of an idealized OEC in acid (29) by utilizing the acid stability and

conductivity of PbO_x. These films showed extended stability in acid at appreciable OER currents and high activity.

We sought to stabilize NiB_i and $(Ni:Fe)B_i$ OECs in acid owing to their exceptional OER activities, especially for the latter (30, 31). We show herein that $NiFePbO_x$ and $NiPbO_x$ films are stable in acid through extended OER electrolysis (>20 h) as compared to NiB_i, NiO_x, and $NiFeO_x$ films, all of which dissolve within minutes under the same conditions. X-ray spectroscopy reveals that the PbO_x-framework is stable under OER conditions in acid. Because the mixed-oxide strategy stabilizes the catalyst, we are able to examine OER in acid, especially the issue of Fe as a promoter of catalysis. Many interesting explanations for the enhanced OER activity of oxidic Ni OER catalysts alloyed with Fe have been posited including active-site Fe species (17, 32–37), near-neighbor Fe effects on OER at Ni resulting from strain on the oxide lattice (38, 39) or as a relay of active oxygen intermediates to Ni (40–42), and Fe-inducing partial-charge-transfer activation of Ni for OER generation (17). We have suggested (43), based on X-ray absorption spectroscopy of $(Ni:Fe)B_i$, that a role of Fe is to act as a Lewis acid, serving to increase the acidity of OH_x (aqua/hydroxo) moieties that are coordinated to nickel, thereby lowering the reduction potential for the $Ni^{3+/4+}$ couple, leading to a greater population of Ni^{4+} in the Fe-doped catalysts. This in turn gives rise to increased oxyl character arising from a $Ni(IV)-{}^-O \leftrightarrow Ni(III)-O^\bullet$ resonance, which leads to facilitated O–O bond formation. Whereas the Lewis acidity [$pK_a = 2.2$ (44)] of Fe^{3+} may be manifested in near-neutral and basic solutions, in more acidic

Significance

Metal-oxide catalysts that do not rely on the critical metals corrode immediately in nonbasic solutions. The development of self-healing offers a design principle to avert corrosion for typical metal oxides in neutral and near-neutral solutions. However, the stabilization of metal-oxide oxygen evolution catalysts (OECs) in acid remains to be a challenge that requires new design principles and strategies. We show here that high activity from OECs may be achieved in acid by embedding catalytic metal-oxide active sites within an acid-stable oxide framework. Specifically, we show that oxidic Ni OECs may be stabilized for extended periods of OER by embedding Ni in the acid-stable oxide framework of PbO_2 polymorphs.
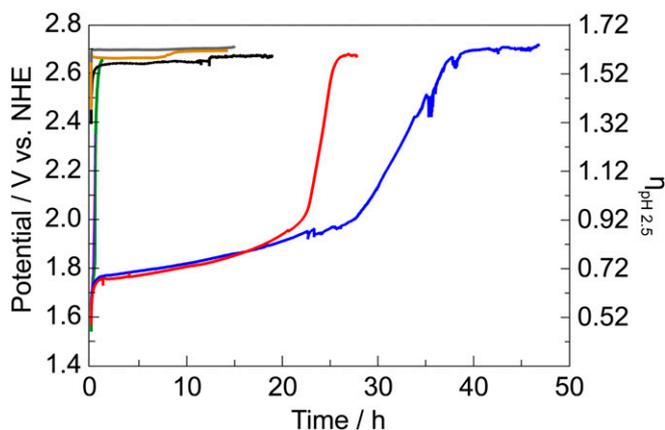
CHEMISTRY

Fig. 1. Electrochemical stability for acidic OER measured by sustained chronopotentiometry at 1 mA cm^{-2} in 0.1 M KP$_i$ + 1.75 M KNO$_3$ pH 2.5 for blank FTO (black), NiB$_i$ (purple), NiFeO$_x$ (green), NiPbO$_x$ (red line), NiFePbO$_x$ (blue line), FePbO$_x$ (mustard line), and PbO$_x$ (gray line). The inflection in the plots indicates film dissolution. The small spikes in potential are due to transient bubble formation on the film surface.

solutions the effect should be mitigated. We indeed show that Fe doping in NiPbO$_x$ shows no enhancement in OER at solution pH values commensurate with the pK_a of Fe^{3+}. Taken together, our findings establish general guidelines for how catalysts may be designed to optimize both OEC activity and stability in acid.

Results

Performance of NiPbO$_x$ and NiFePbO$_x$ Films in Acid. NiFePbO$_x$ and NiPbO$_x$ films were electrodeposited at a constant anodic potential of 1.3 V vs. NHE from aqueous solutions containing the appropriate metal salts and methylphosphonate (MeP$_i$) buffer at pH 8, similar to previously published methods (*SI Appendix*, Fig. S1) (29); PbO$_x$ and FePbO$_x$ films were similarly prepared. The deposition times for all films were chosen so as to yield ~250 nmol in total metal loading as confirmed by inductively coupled plasma mass spectrometry (ICP-MS) (*SI Appendix*, Table S1). The as-deposited NiPbO$_x$ films contain equal parts Ni (50.3 ± 0.3 mol %) and Pb (49.7 ± 1.2 mol %). Likewise, the as-deposited NiFePbO$_x$ films also contain approximately equal parts Ni (30.1 ± 0.6 mol %), Fe (30.9 ± 1.2 mol %), and Pb (39.0 ± 0.8 mol %).

The morphology of each film was examined by scanning electron microscopy (SEM) (*SI Appendix*, Fig. S2). PbO$_x$ films appear to be filament-like whereas NiPbO$_x$ appear to be more nanoparticlelike in morphology; comparing NiPbO$_x$ and NiFePbO$_x$, the addition of Fe appears to change the morphology by decreasing the size of the nanoparticle structures. Average particle diameters of ~150 and ~70 nm are observed for NiPbO$_x$ and NiFePbO$_x$, respectively. Energy-dispersive X-ray spectroscopy (EDS) mapping shows a uniform distribution of elements throughout the surface of all films (*SI Appendix*, Fig. S3). The amorphous nature of PbO$_x$-templated films precluded the use of X-ray diffraction as a characterization tool.

The stabilities of PbO$_x$-based films (mixed-metal-oxide films employing a lead-oxide lattice framework) were evaluated with chronopotentiometry in 0.1 M KP$_i$ + 1.75 M KNO$_3$ solutions at pH 2.5 (Fig. 1). Electrodeposited films were immersed in stirred solutions and held at a constant current density of 1 mA cm^{-2} where, after a brief capacitance period, only OER was sustained. The applied potentials required to maintain 1 mA cm^{-2} of OER (V$_{1mA}$) for NiFePbO$_x$ and NiPbO$_x$ films initially stabilize at a value well below that of blank fluorinated tin oxide (FTO) (*SI Appendix*, Fig. S4A). This potential is maintained for >20 h before rapidly rising to the value for OER on FTO. Both NiFePbO$_x$

and NiPbO$_x$ films have superior acid stability over NiO$_x$, NiFeO$_x$, and NiB$_i$ films, which immediately dissolve in acidic conditions (Fig. 1 and *SI Appendix*, Fig. S4B), whereas PbO$_x$ and FePbO$_x$ perform OER at a V$_{1mA}$ similar to blank FTO. Addition of Fe into NiPbO$_x$ increases the stability of the film in acid (Fig. 1 and *SI Appendix*, Fig. S4B) but does not influence V$_{1mA}$ (*SI Appendix*, Fig. S4A). To confirm that all electrons consumed are used for OER, the faradaic efficiency of NiFePbO$_x$ was measured under operation at 1 mA cm^{-2} by chronopotentiometry in 0.1 M KP$_i$ + 1 M KNO$_3$ pH 2.5. The evolved oxygen was directly measured by gas chromatography from a gas-tight electrochemical cell and the O$_2$ concentration was sampled every 20 min after an initial 30 min of purging the gas headspace with Ar. The faradaic efficiency of NiFePbO$_x$ for oxygen generation was 103 ± 3% (*SI Appendix*, Fig. S5).

To determine the activity of NiFePbO$_x$ and NiPbO$_x$ films for OER, Tafel plots were measured in 0.1 M KP$_i$ + 1 M KNO$_3$ pH 2.5 buffer. Both NiFePbO$_x$ and NiPbO$_x$ films display a similar Tafel slope of ~90 mV/dec (Fig. 2), which is similar to that of NiFePbO$_x$ at pH 7 (*SI Appendix*, Fig. S6) and NiO$_x$ in near-neutral and basic conditions (15–17). Increasing the amount of Fe in the film relative to Ni results in an increase in the Tafel slope of NiFePbO$_x$ films (*SI Appendix*, Fig. S7A) with a concomitant increase in V$_{1mA}$ (*SI Appendix*, Fig. S7B). Additionally, cyclic voltammograms performed with NiPbO$_x$ and NiFePbO$_x$ films in 0.1 M KP$_i$ + 1 M KNO$_3$ pH 2.5 buffer show that the OER activity of the two films is very similar (*SI Appendix*, Fig. S13). A slight reduction in the size of the precatalytic redox feature for the NiFePbO$_x$ film is observed, likely due to the reduced Ni content of the Fe-containing film. The OER enhancement of Fe on Ni is thus not observed in NiFePbO$_x$ under acidic conditions.

X-Ray Absorption Spectroscopy of PbO$_x$ Based Films. X-ray absorption spectroscopy (XAS) was utilized to assess the *in situ* geometric and electronic structure of NiFePbO$_x$ and to assess changes to the PbO$_x$ lattice that may be induced by the addition of Ni and Fe centers. The Pb L$_3$ edge of *in situ* NiFePbO$_x$ (operated at 1.7 V in 0.1 M KP$_i$ and 1 M KNO$_3$ pH 2.5 buffer) is given in Fig. 3A, along with data for Pb(II)O, Pb(II,IV)$_3$O$_4$, and Pb(IV)O$_2$. Depending on the oxidation state, the Pb L$_3$ edge comprises three or four transitions from the Pb 2$p_{3/2}$ state (45, 46). Band (I) is present in Pb(IV)-containing compounds and arises from a Pb 2$p_{3/2} \rightarrow 6s_{1/2}$ transition [oxidation of Pb(II) to Pb(IV) opens up this dipole-allowed transition that is not present in Pb(II) compounds due to the filled 6s^2 electronic configuration]. Thus, the *in situ* L$_3$-edge XAS data support a Pb(IV) oxidation state in NiFePbO$_x$ under OER conditions, as expected based on the Pourbaix diagram of lead. There are some differences between the Pb(IV)O$_2$ standard and *in situ* NiFePbO$_x$ in
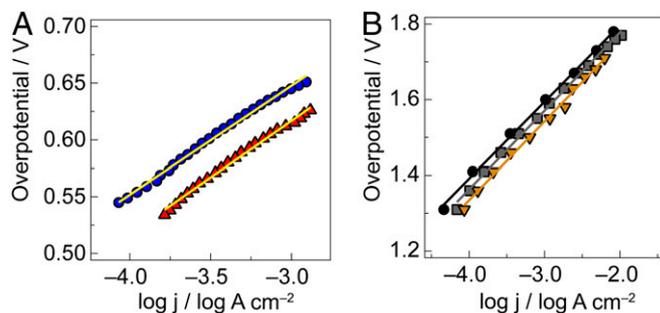

Fig. 2. Tafel plots of oxygen evolution in 0.10 M KP$_i$ + 1 M KNO$_3$ pH 2.5 of (*A*) NiPbO$_x$ (red triangles, 87 ± 5 mV/dec) and NiFePbO$_x$ (blue dots, 89 ± 6 mV/dec) (*B*) PbO$_x$ (gray squares, 206 ± 2 mV/dec), FePbO$_x$ (mustard triangles, 205 ± 3 mV/dec), and blank FTO (black dots, 201 ± 2 mV/dec).
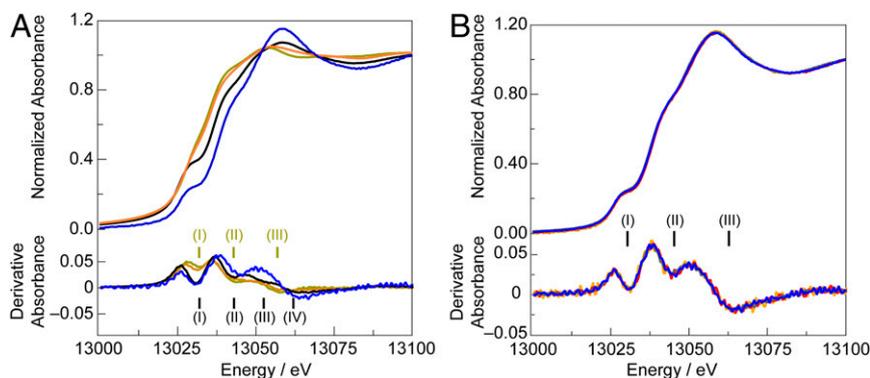
Li et al.

Fig. 3. (*A*) Pb L$_3$-edge X-ray absorption spectra and corresponding for NiFePbO$_x$ under OER (blue line), and Pb oxide standards: PbO (olive line), Pb$_3$O$_4$ (orange line), and PbO$_2$ (black line). (*B*) Pb L$_3$-edge X-ray absorption spectra with related derivative absorption for films operating in 0.1 M KP$_i$ + 1M KNO$_3$ pH 2.5 at 1.9 V: PbO$_x$ (gray), NiPbO$_x$ (red), FePbO$_x$ (mustard), and NiFePbO$_x$ (blue).

terms of intensity distributions over the higher-energy transitions making up the L$_3$ edge. As these transitions involve final states with mixed Pb $6p_{1/2}/d_{3/2}$ and Pb $6d$ nonbonding and antibonding character, this energy region may reflect partial covalent interaction between unoccupied Pb $6d$ and occupied Ni and/or Fe orbitals. All PbO$_x$ films operating under anodic potentials (1.7 V) in acid exhibit similar Pb L$_3$-edge XAS spectra (Fig. 3*B*). Moreover, the presence of Ni and/or Fe in PbO$_x$ does not appear to significantly influence the L$_3$-edge energies or overall spectral shape.

The PbO$_x$ framework was also examined by X-ray photoelectron spectroscopy (XPS). Addition of any other metal into the PbO$_x$ framework results in a shift of the Pb $4f$ peaks toward higher binding energies (Fig. 4*A*). The Pb $4f$ binding energies for FePbO$_x$ and NiFePbO$_x$ appear roughly aligned, and NiPbO$_x$ has the highest Pb $4f$ binding energies. The O $1s$ XPS spectra of PbO$_x$ show peaks at ~529 eV, a major peak at ~530 eV, and a small shoulder at ~532 eV (Fig. 4*B*). The peak at 529 eV disappears when any metal is added into the PbO$_x$ framework. FePbO$_x$ and NiFePbO$_x$ films all have similar O $1s$ spectra consisting of one dominant peak at 530.7 eV and a small shoulder at 532 eV. For PbO$_x$ and NiPbO$_x$ there is a dominant peak at 530 eV and a prominent shoulder at 532 eV; the latter is diminished with the addition of Fe into the framework. The Pb $4f$ and O $1s$ XPS spectra of PbO$_x$ films do not show any significant changes in binding energy or shape for samples that were held at 1.45 V versus those held at 2.00 V. This indicates that the observed shifts in Pb $4f$ binding energy are not the result of the various potentials (1.45–2.0 V) applied to PbO$_x$-based films. Consistent with XAS results, the addition of Fe (~11 mol % Fe) into the NiPbO$_x$ film yielded no changes in the XPS spectrum in the Ni $2p$ region (*SI Appendix*, Fig. S8).

To understand the electronic changes occurring at the metal and oxygen centers throughout operation of OER in acid, *ex situ* XAS and XPS spectra of NiFePbO$_x$ were examined. Under OER conditions in acid, the influence of Fe on Ni centers within the PbO$_x$ framework is minimal. The Ni K edge in the XAS spectrum of NiFePbO$_x$ is slightly red-shifted compared to that of NiPbO$_x$ (*SI Appendix*, Fig. S9; 12.9 ± 5.2% Fe), similar to what has been observed for NiFeO$_x$ operating OER in base (47) and NiFeB$_i$ in near-neutral buffers (43). For the case of the PbO$_x$ lattice, the XPS spectra of Pb $4f$, Ni $2p$, and O $1s$ in NiFePbO$_x$ were tracked over several hours until film dissolution in 0.1 M KP$_i$ + 1 M KNO$_3$ pH 2.5 (*SI Appendix*, Fig. S10). The Pb $4f$ peaks are shifted toward higher energies in NiFePbO$_x$ films that operate 1 mA cm^{-2} of OER for 40 h (past film stability) versus those films operating 1 mA cm^{-2} of OER for 10 min. The O $1s$ peaks are also shifted toward higher energies, and intensity of the peak at 532 eV increases after 40 h of OER. The amount of Ni left on

the surface of the FTO substrate is below detection level for XPS analysis. This suggests that the shift toward higher binding energies is likely due to the oxidation of metal centers at the significantly higher potential (2.7 V) required to achieve 1 mA cm^{-2} of OER after film dissolution.

Catalyst Composition throughout OER. We compared the elemental composition of as-deposited PbO$_x$-based films with films that had deactivated following 40 h of OER at 1 mA cm^{-2} in 0.1 M KP$_i$ + 1 M KNO$_3$ pH 2.5 (*SI Appendix*, Fig. S11 and Table S1). After performing OER for 40 h, films exhibit a notable loss of Ni and Fe, which is expected given their propensity to dissolve in acid as predicted by the Pourbaix diagram. NiPbO$_x$ films show an ~99% loss of Ni relative to as-deposited films, while NiFePbO$_x$ films show ~96 and ~88% loss of Ni and Fe, respectively, relative to as-deposited films. Both NiPbO$_x$ and NiFePbO$_x$ films have similar Pb loading (relative to as-deposited films) after 40 h. To observe changes in film morphology and structure during operation, the elemental maps of the Pb M edge on NiFePbO$_x$ film surfaces were tracked at different time points during operation of 1 mA cm^{-2} of OER in 0.1 M KP$_i$ + 1 M KNO$_3$ pH 2.5 (Fig. 5 and *SI Appendix*, Fig. S12). Mapping of the Pb M edge on these film surfaces reveals a systematic etching of the PbO$_x$ lattice; the film starts out with a uniform Pb distribution that breaks apart to form islands that become more separated over time.

Discussion

NiFePbO$_x$ and NiPbO$_x$ OER Activity in Acid. NiPbO$_x$ and NiFePbO$_x$ films have a homogeneous dispersion of metal centers (*SI*
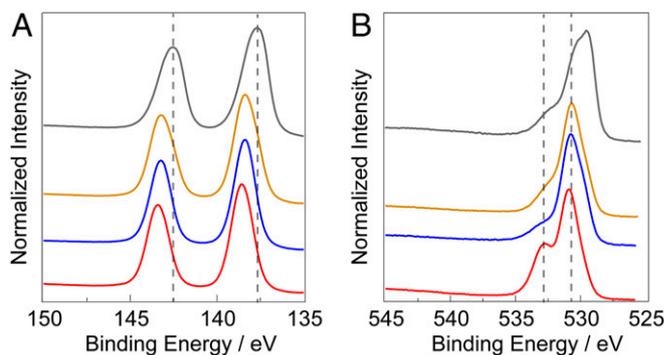

Fig. 4. High-resolution XPS spectra of (*A*) Pb $4f$ and (*B*) O $1s$ in catalyst films after maintaining an OER current of 1 mA cm^{-2} in 0.1 M KP$_i$ + 1 M KNO$_3$ pH 2.5 for 10 min: PbO$_x$ (gray line), FePbO$_x$ (mustard line), NiFePbO$_x$ (blue line), and NiPbO$_x$ (red line).
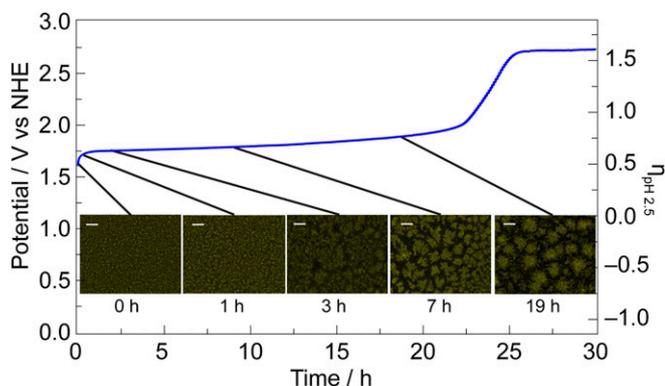
Li et al.

Fig. 5. SEM mapping of Pb M edge (yellow contrast) on NiFePbO$_x$ film surface after performing OER at 1 mA cm^{-2} in 0.1 M KP$_i$ + 1 M KNO$_3$ pH 2.5 buffer for 0, 1, 3, 7, and 19 h. Chronopotentiometry curve is illustrated in blue. Intensities of the Pb M-edge signal are normalized within each image.

Appendix, Fig. S3) and exhibit extended stability in acid while maintaining 1 mA cm^{-2} of OER (Fig. 1). The addition of Fe into the NiFePbO$_x$ framework extends the film stability by ~8 h in contrast to NiB$_i$, NiO$_x$, and NiFeO$_x$ films, all of which dissolve within the first few minutes of OER operation in acid (*SI Appendix*, Fig. S3B).

While Fe has been shown to improve the OER activity of NiO$_x$ films in base (17, 48), it does not appear to play a significant role in the enhancement of OER in acid. Both NiFePbO$_x$ and NiPbO$_x$ yield a Tafel slope of ~90 mV/dec in acidic conditions (Fig. 3A and *SI Appendix*, Fig. S7A), which matches that exhibited by pure NiO$_x$ in near-neutral and basic conditions (17, 48). Additionally, both the exchange current density and the V$_{1mA}$ scale with Ni rather than Fe content (*SI Appendix*, Fig. S7). The absence of Fe enhancement in acid is inconsistent with the proposed role of Fe as the active site for OER in Ni:Fe oxide films (17, 32–36). ICP-MS analysis of NiFePbO$_x$ films shows an ~30 mol % Ni and ~30 mol % Fe composition. Elemental mapping by SEM/EDS illustrates a uniform distribution of metals on the film surface (*SI Appendix*, Fig. S3D). Furthermore, when operated in near-neutral (pH 9.2) solutions, NiFePbO$_x$ yields a lower Tafel slope of 48 mV/dec (*SI Appendix*, Fig. S6B). These three observations suggest that Fe centers are likely

proximate to Ni in the PbO$_x$ matrix and are thus not prohibitively diluted to prevent Fe enhancement of OER as suggested by active-site models. It is noteworthy that the observed 48-mV/dec Tafel slope for NiFePbO$_x$ at pH 9.2 is similar to that of NiB$_i$ (16), suggesting that the nature of the OER active sites in these films at near-neutral pH are similar to NiB$_i$. Rather, the absence of an Fe effect on OER is consistent with the proposal of Fe's role as a superior Lewis acid promoter of OER (43). The percent of Fe^{3+} doping promotes the formation of formal Ni^{4+}, which in turn directly correlates with an enhanced activity of the catalyst in promoting OER. This observation has been ascribed to the presence of Lewis acidic Fe^{3+} serving to increase the acidity of OH$_x$ (aqua/hydroxo) moieties that are coordinated to nickel, thereby lowering the reduction potential for the Ni$^{3+/4+}$ couple and engendering a greater population of Ni^{4+} in the Fe-doped catalysts. Computation and experiment show Fe^{3+} to be the most acidic transition metal ion with a pK_a = 2.2 for the deprotonation of coordinated water (44). Thus, the Lewis acidity of Fe^{3+} will be manifested in the enhancement for OER performed in near-neutral conditions but not under the conditions reported here (pH = 2.5) as the pK_a of Fe^{3+} is commensurate with the solution acidity.

Structural Analysis of PbO$_x$ Films. The similarity of Pb L$_3$-edge XAS data shown in Fig. 3 suggests that the Pb(IV)O$_2$ host structure is not greatly perturbed by Ni and Fe doping. Such behavior has been observed previously for doped PbO$_2$ matrices, which retain the PbO$_2$ structure upon doping (49–51). PbO$_2$ films prepared by electrodeposition have been shown to yield mixtures of both orthorhombic (α) and tetragonal (β) polymorphs (52–54) (*SI Appendix*, Fig. S14); however, the similarity of Pb–O and Pb–Pb bond lengths for these two polymorphs (55–57) does not allow them to be distinguished by XAS. More insight into the nature of the host structure of NiPbO$_x$ and NiFePbO$_x$ films is offered by XPS spectra. The Pb 4f peaks shift toward higher binding energies with the addition of Ni and Fe into the lattice (Fig. 3A). These shifts are not the results of differences in applied potential as the Pb 4f and O 1s spectra of PbO$_x$ held at 1.45 and 2.00 V are virtually identical and they do not appear to correlate with film stability in acid. These results suggest that Pb oxidation state alone does not dictate Pb 4f peak positions, which may be influenced by distortion about Pb induced by metal ion doping.
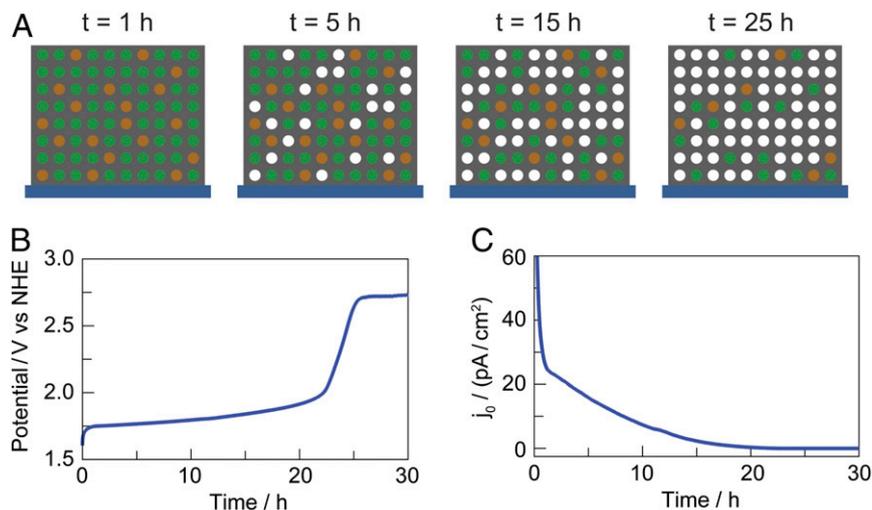

Fig. 6. (A) Schematic illustrating dissolution of metal centers in NiFePbO$_x$ film (Pb: gray dots; Ni: green dots; and Fe: brown dots). Over the course of operation, Ni and Fe are leached from the more inert conductive PbO$_x$ matrix. Corresponding (B) potential required to maintain 1 mA cm^{-2} of OER in acid. (C) Exchange-current density for the catalyst film calculated from chronopotentiometry data.

The dominant peak at ~530 eV and smaller peak at ~532 eV in the PbO$_x$ O 1s spectra are attributed to lattice and hydroxyl oxygens, respectively (58). NiPbO$_x$ exhibits a more prominent hydroxyl peak than observed in NiFePbO$_x$ (Fig. 4B), in accordance with the greater stability of NiFePbO$_x$ in acid. We surmise that as the PbO$_x$ lattice becomes etched by acid, more edge sites are generated, resulting in an increase in hydroxyl peaks in the O 1s spectra. In support of this contention, the hydroxyl peak of NiFePbO$_x$ films becomes more prominent (*SI Appendix*, Fig. S10B) with operation of the film in acid over the course of 40 h.

Mechanism of Acid Dissolution in PbO$_x$-Based OECs. Although dissolution is expected for metal oxides in acid (NiO$_x$ FeO$_x$), once the metal ions are embedded in an acid-stable PbO$_x$ matrix, stability is engendered for extended periods of time, after which the catalyst overpotential rises quickly as evidenced by the relatively sharp inflection point in the chronopotentiometry curves (Fig. 1). This sharp increase in operating potential under constant current conditions may reflect the exponential relationship between current and potential. Assuming that the current passed is the sum of contributions from the catalyst and the underlying FTO substrate, the following expression describes the total current:

$$j_{tot} = j_{0(\mathrm{Cat})}10^{(\eta/m_{\mathrm{Cat}})} + j_{0(\mathrm{FTO})}10^{(\eta/m_{\mathrm{FTO}})}, \qquad \textbf{[1]}$$

where $j_{0(\mathrm{Cat})}$ and $j_{0(\mathrm{FTO})}$ are the exchange-current densities for the catalyst film and FTO, respectively, m_{Cat} and m_{FTO} are the Tafel slopes for the catalyst film and FTO, respectively, and η is the applied overpotential. In this regard, the exchange-current density of the catalyst can be used as a proxy for the number of intact active sites in the film.

If we assume that the current from FTO and the Tafel slope for the catalyst remain constant over the course of the experiment, the exchange-current density of the catalyst as a function of applied overpotential over the course of a constant-current electrolysis experiment is given by

$$j_{0(\mathrm{Cat})} = 10^{(-\eta/m_{\mathrm{Cat}})}\Big(j_{tot} - j_{0(\mathrm{FTO})}10^{(\eta/m_{\mathrm{FTO}})}\Big). \qquad \textbf{[2]}$$

Using this equation, the potential vs. time curves obtained in our studies may be recast as exchange-current vs. time plots, which better illustrate the number of active sites in a given catalyst film over the course of electrolysis. Fig. 6 displays such a plot for a NiFePbO$_x$ film. Inspection of the exchange-current density as a function of time reveals a steady loss of active sites from the film over the course of electrolysis, until the activity of the catalyst drops below that of the underlying FTO substrate.

A catalyst dissolution mechanism in which active sites are steadily lost over the course of electrolysis is supported by ICP data; comparison of metal content in as-deposited films versus after dissolution (after the inflection point in V$_{1\mathrm{mA}}$) shows a dramatic reduction in Fe and Ni content (*SI Appendix*, Fig. S11). The dissolution of these metal centers indicates that, even when embedded into an acid-stable PbO$_x$ lattice, the 3d metal-oxide ligation sphere is not fully protected from protonation at the edge sites, which in turn exposes more edge sites for continued film dissolution. Such a dissolution mechanism is supported by the growth in hydroxyl oxygen peaks in the O 1s spectra of NiFePbO$_x$ films over operation of OER in acid. We note that accelerated metal leaching occurs from this class of oxidic metallate OER catalysts in neutral solution when they are held at open-circuit potential (59) as an applied electrochemical potential is needed to extend the lifetime of these catalysts via self-healing mechanisms (60). As we show here, the stability offered by self-healing is further augmented by the appropriate choice of a host lattice for catalytic active sites.

Conclusion

Metal oxides are notoriously unstable in nonbasic conditions, especially when employed as catalysts for OER. The four-electron oxidation of water to oxygen is accompanied by the release of four protons. In basic solution, the concentration of OH$^-$ is appreciable and the protons released from water splitting may be neutralized. However, in water at pH 7 or near-neutral conditions, the concentration of OH$^-$ is low and the metal oxide is the strongest base as reflected in the Lux classification of bases (61). Hence typical metal oxides are prone to corrosion by the leaching of metal ions and dissolution of the oxide. To overcome corrosion in water, we have developed self-healing catalysts that are able to self-assemble at applied potentials less than that needed for catalyst turnover (60). Solution pH provides a convenient handle for controlling the potential of these two processes, and as we have shown, may be exploited in the stabilization of catalyst in neutral and near-neutral water. However, at acidic pHs, self-healing is difficult to implement. Hence, new design approaches are needed for performing OEC in acid. To this end, we show here that template, acid-stable frameworks provide a viable milieu to extend the stability of metal oxides that otherwise corrode in acid. The mixed-metal-oxide design is bolstered by the flexibility with which one can incorporate disparate metal centers that serve as the 1) active center for oxygen evolution, 2) acid stabilizing framework, and 3) OER activity enhancers. To this end, we illustrate here that the high activity of oxidic Ni catalyst may be recapitulated in acid over appreciable periods of OEC when incorporated within an acid-stable PbO$_x$ matrix. *In situ* and *ex situ* spectroscopic X-ray techniques reveal that oxidic Ni-PbO$_x$ OER catalyst is a compact structure that mitigates attack by acid. Noting that practical electrolyzers require sustained OER activity for considerable operation times (62), our results offer a design element and an inroad for creating acid-stable catalysts that can promote water splitting at high activities.

Besides the practical aspect of enhanced stability, the ability to examine oxidic Ni:Fe vs. Ni OER in acid provides insight into the role of Fe in promoting OER by nickel oxide catalysts. Koper and coworkers have shown the importance of deprotonating γ-NiOOH in promoting OER (63). In native Ni oxy(hydroxides), this deprotonation can only occur under basic conditions. However, in near-neutral solutions (pH 9–11), the presence of the Lewis acidic Fe^{3+} may serve to increase the acidity of OH$_x$ (aqua/hydroxo) moieties that are coordinated to nickel, thereby facilitating OER. In contrast, in acidic solutions of pH = 2.5, the Lewis acidity of Fe^{3+} is abrogated and hence, as we report here, the presence of Fe^{3+} does not lead to enhancements in OER. The present work provides further support for the role of Fe as a Lewis acid in promoting OER. These results do not exclude the existence of multiple active sites, as has been proposed by others (40, 64), in which different active sites may promote catalysis in different pH regimes.

CHEMISTRY

1. N. S. Lewis, D. G. Nocera, Powering the planet: Chemical challenges in solar energy utilization. *Proc. Natl. Acad. Sci. U.S.A.* **103**, 15729–15735 (2006).

2. T. R. Cook *et al.*, Solar energy supply and storage for the legacy and nonlegacy worlds. *Chem. Rev.* **110**, 6474–6502 (2010).

3. S. Chu, A. Majumdar, Opportunities and challenges for a sustainable energy future. *Nature* **488**, 294–303 (2012).

4. N. S. Lewis, D. G. Nocera, The solar opportunity. *Bridge* **46**, 41–47 (2015).

5. H. Arakawa *et al.*, Catalysis research of relevance to carbon management: Progress, challenges, and opportunities. *Chem. Rev.* **101**, 953–996 (2001).

6. D. G. Nocera, Solar fuels and solar chemicals industry. *Acc. Chem. Res.* **50**, 616–619 (2017).

7. C. Liu, B. C. Colón, M. Ziesack, P. A. Silver, D. G. Nocera, Water splitting-biosynthetic system with CO_2 reduction efficiencies exceeding photosynthesis. *Science* **352**, 1210–1213 (2016).

8. R. Eisenberg, H. B. Gray, Preface on making oxygen. *Inorg. Chem.* **47**, 1697–1699 (2008).

9. F. Liu *et al.*, Mechanisms of water oxidation from the blue dimer to photosystem II. *Inorg. Chem.* **47**, 1727–1752 (2008).

10. H. Dau *et al.*, The mechanism of water oxidation: From electrolysis via homogeneous to biological catalysis. *ChemCatChem* **2**, 724–761 (2010).

11. M. W. Kanan, D. G. Nocera, In situ formation of an oxygen-evolving catalyst in neutral water containing phosphate and Co^{2+}. *Science* **321**, 1072–1075 (2008).

12. Y. Surendranath, M. W. Kanan, D. G. Nocera, Mechanistic studies of the oxygen evolution reaction by a cobalt-phosphate catalyst at neutral pH. *J. Am. Chem. Soc.* **132**, 16501–16509 (2010).

13. J. B. Gerken *et al.*, Electrochemical water oxidation with cobalt-based electrocatalysts from pH 0-14: The thermodynamic basis for catalyst structure, stability, and activity. *J. Am. Chem. Soc.* **133**, 14431–14442 (2011).

14. K. Klingan *et al.*, Water oxidation by amorphous cobalt-based oxides: Volume activity and proton transfer to electrolyte bases. *ChemSusChem* **7**, 1301–1310 (2014).

15. M. Dincă, Y. Surendranath, D. G. Nocera, Nickel-borate oxygen-evolving catalyst that functions under benign conditions. *Proc. Natl. Acad. Sci. U.S.A.* **107**, 10337–10341 (2010).

16. D. K. Bediako, Y. Surendranath, D. G. Nocera, Mechanistic studies of the oxygen evolution reaction mediated by a nickel-borate thin film electrocatalyst. *J. Am. Chem. Soc.* **135**, 3662–3674 (2013).

17. L. Trotochaud, S. L. Young, J. K. Ranney, S. W. Boettcher, Nickel-iron oxyhydroxide oxygen-evolution electrocatalysts: The role of intentional and incidental iron incorporation. *J. Am. Chem. Soc.* **136**, 6744–6753 (2014).

18. D. Kang *et al.*, Electrochemical synthesis of photoelectrodes and catalysts for use in solar water splitting. *Chem. Rev.* **115**, 12839–12887 (2015).

19. I. Roger, M. D. Symes, First row transition metal catalysts for solar-driven water oxidation produced by electrodeposition. *J. Mater. Chem. A* **4**, 6724–6741 (2016).

20. I. Roger, M. A. Shipman, M. D. Symes, Earth-abundant catalysts for electrochemical and photoelectrochemical water splitting. *Nat. Rev. Chem.* **1**, 1–13 (2017).

21. B. Seger, K. Vinodgopal, P. V. Kamat, Proton activity in nafion films: Probing exchangeable protons with methylene blue. *Langmuir* **23**, 5471–5476 (2007).

22. D. G. Nocera, The artificial leaf. *Acc. Chem. Res.* **45**, 767–776 (2012).

23. N. Bunkin *et al.*, Study of the phase states of water close to Nafion interface. *Water* **4**, 129–154 (2013).

24. S. Trasatti, Electrocatalysis by oxides-attempt at a unifying approach. *J. Electroanal. Chem.* **111**, 125–131 (1980).

25. Y. Surendranath, D. G. Nocera, Oxygen evolution reaction chemistry of oxide–based electrodes. *Prog. Inorg. Chem.* **57**, 505–560 (2011).

26. M. Huynh, D. K. Bediako, D. G. Nocera, A functionally stable manganese oxide oxygen evolution catalyst in acid. *J. Am. Chem. Soc.* **136**, 6002–6010 (2014).

27. M. Huynh, D. K. Bediako, Y. Liu, D. G. Nocera, Nucleation and growth mechanisms of an electrodeposited manganese oxide oxygen evolution catalyst. *J. Phys. Chem. C* **118**, 17142–17152 (2014).

28. M. Huynh, C. Shi, S. J. L. Billinge, D. G. Nocera, Nature of activated manganese oxide for oxygen evolution. *J. Am. Chem. Soc.* **137**, 14887–14904 (2015).

29. M. Huynh, T. Ozel, C. Liu, E. C. Lau, D. G. Nocera, Design of template-stabilized active and earth-abundant oxygen evolution catalysts in acid. *Chem. Sci.* **8**, 4779–4794 (2017).

30. L. Trotochaud, J. K. Ranney, K. N. Williams, S. W. Boettcher, Solution-cast metal oxide thin film electrocatalysts for oxygen evolution. *J. Am. Chem. Soc.* **134**, 17253–17261 (2012).

31. D. K. Bediako *et al.*, Structure-activity correlations in a nickel-borate oxygen evolution catalyst. *J. Am. Chem. Soc.* **134**, 6801–6809 (2012).

32. M. W. Louie, A. T. Bell, An investigation of thin-film Ni-Fe oxide catalysts for the electrochemical evolution of oxygen. *J. Am. Chem. Soc.* **135**, 12329–12337 (2013).

33. B. M. Hunter *et al.*, Highly active mixed-metal nanosheet water oxidation catalysts made by pulsed-laser ablation in liquids. *J. Am. Chem. Soc.* **136**, 13118–13121 (2014).

34. D. Friebel *et al.*, Identification of highly active Fe sites in (Ni,Fe)OOH for electrocatalytic water splitting. *J. Am. Chem. Soc.* **137**, 1305–1313 (2015).

35. S. Klaus, Y. Cai, M. W. Louie, L. Trotochaud, A. T. Bell, Effects of Fe electrolyte impurities on $Ni(OH)_2$/NiOOH structure and oxygen evolution activity. *J. Phys. Chem. C* **119**, 7243–7254 (2015).

36. J. R. Swierk, S. Klaus, L. Trotochaud, A. T. Bell, T. D. Tilley, Electrochemical study of the energetics of the oxygen evolution reaction at nickel iron (oxy)hydroxide catalysts. *J. Am. Chem. Soc.* **119**, 19022–19029 (2015).

37. J. M. P. Martirez, E. A. Carter, Unraveling oxygen evolution on iron-doped β-nickel oxyhydroxide: The key role of highly active molecular-like sites. *J. Am. Chem. Soc.* **141**, 693–705 (2019).

38. R. D. L. Smith *et al.*, Geometric distortions in nickel (oxy)hydroxide electrocatalysts by redox inactive iron ions. *Energy Environ. Sci.* **11**, 2476–2485 (2018).

39. E. P. Alsaç, A. Whittingham, Y. Liu, R. D. L. Smith, Probing the role of internalized geometric strain on heterogeneous electrocatalysis. *Chem. Mater.* **31**, 7522–7530 (2019).

40. S. Lee, K. Banjac, M. Lingenfelder, X. Hu, Oxygen isotope labeling experiments reveal different reaction sites for the oxygen evolution reaction on nickel and nickel iron oxides. *Angew. Chem. Int. Ed. Engl.* **58**, 10295–10299 (2019).

41. H. Xiao, H. Shin, W. A. Goddard III, Synergy between Fe and Ni in the optimal performance of (Ni,Fe)OOH catalysts for the oxygen evolution reaction. *Proc. Natl. Acad. Sci. U.S.A.* **115**, 5872–5877 (2018).

42. H. Shin, H. Xiao, W. A. Goddard III, In silico discovery of new dopants for Fe-doped Ni oxyhydroxide ($Ni_{1-x}Fe_xOOH$) catalysts for oxygen evolution reaction. *J. Am. Chem. Soc.* **140**, 6745–6748 (2018).

43. N. Li *et al.*, Influence of iron doping on tetravalent nickel content in catalytic oxygen evolving films. *Proc. Natl. Acad. Sci. U.S.A.* **114**, 1486–1491 (2017).

44. S. V. Jerome, T. F. Hughes, R. A. Friesner, Accurate pK_a prediction in first-row hexaaqua transition metal complexes using the B3LYP-DBLOC method. *J. Phys. Chem. B* **118**, 8008–8016 (2014).

45. Y. H. Yu, T. Tyliszczak, A. P. Hitchcock, Pb L_3 EXAFS and near-edge studies of lead metal and lead oxides. *J. Phys. Chem. Solids* **51**, 445–451 (1990).

46. K. J. Rao, J. A. Wong, XANES investigation of the bonding of divalent lead in solids. *J. Chem. Phys.* **81**, 4832–4843 (1984).

47. M. K. Bates, Q. Jia, H. Doan, W. Liang, S. Mukerjee, Charge-transfer effects in Ni–Fe and Ni–Fe–Co mixed-metal oxides for the alkaline oxygen evolution reaction. *ACS Catal.* **6**, 155–161 (2016).

48. D. A. Corrigan, The catalysis of the oxygen evolution reaction by iron impurities in thin film nickel oxide electrodes. *J. Electrochem. Soc.* **134**, 377–384 (1987).

49. I.-H. Yeo, S. Kim, R. Jacobson, D. C. Johnson, Electrocatalysis of anodic oxygen transfer reactions: Comparison of structural data with electrocatalytic phenomena for bismuth-doped lead dioxide. *J. Electrochem. Soc.* **136**, 1395–1401 (1989).

50. A. B. Velichenko, R. Amadelli, E. A. Baranova, D. V. Girenko, F. I. Danilov, Electrodeposition of Co-doped lead dioxide and its physicochemical properties. *J. Electroanal. Chem.* **527**, 56–64 (2002).

51. S. Ai, M. Gao, W. Zhang, Z. Sun, L. Jin, Preparation of fluorine-doped lead dioxide modified electrodes for electroanalytical applications. *Electroanal.* **15**, 1403–1409 (2003).

52. I. Petersson, E. Ahlberg, B. Berghult, Parameters influencing the ratio between electrochemically formed α- and β-PbO_2. *J. Power Sources* **76**, 98–105 (1998).

53. D. Zhou, L. Gao, Effect of electrochemical preparation methods on structure and properties of PbO_2 anodic layer. *Electrochim. Acta* **53**, 2060–2064 (2007).

54. P. Rüetschi, B. D. Cahan, Electrochemcial properties of PbO_2 and the anodic corrosion of lead and lead alloys. *J. Electrochem. Soc.* **105**, 369–377 (1958).

55. S. R. Ellis, N. A. Hampson, M. C. Ball, F. Wilkinson, The lead dioxide electrode. *J. Appl. Electrochem.* **16**, 159–167 (1986).

56. W. Mindt, Electrical properties of electrodeposited PbO_2 films. *J. Electrochem. Soc.* **116**, 1076–1080 (1969).

57. X. Li, D. Pletcher, F. C. Walsh, Electrodeposited lead dioxide coatings. *Chem. Soc. Rev.* **40**, 3879–3894 (2011).

58. K. S. Kim, T. J. O'Leary, N. Winograd, X-ray photoelectron spectra of lead oxides. *Anal. Chem.* **45**, 2214–2218 (1973).

59. D. A. Lutterman, Y. Surendranath, D. G. Nocera, A self-healing oxygen-evolving catalyst. *J. Am. Chem. Soc.* **131**, 3838–3839 (2009).

60. C. Costentin, D. G. Nocera, Self-healing catalysis in water. *Proc. Natl. Acad. Sci. U.S.A.* **114**, 13380–13384 (2017).

61. H. Lux, "Säuren" und "basen" im schmelzfluss: Die bestimmung der sauerstoffionenkonzentration. *Ztschr Elektrochem* **45**, 303–309 (1939).

62. O. Schmidt *et al.*, Future cost and performance of water electrolysis: An expert elicitation study. *Int. J. Hydrogen Energy* **42**, 30470–30492 (2017).

63. O. Diaz-Morales, D. Ferrus-Suspedra, M. T. M. Koper, The importance of nickel oxyhydroxide deprotonation on its activity towards electrochemical water oxidation. *Chem. Sci.* **7**, 2639–2645 (2016).

64. S. Lee, L. Bai, X. Hu, Deciphering iron-dependent activity in oxygen evolution catalyzed by nickel–iron layered double hydroxide. *Angew. Chem. Int. Ed. Engl.* **59**, 8072–8077 (2020).